Phase contrast imaging simulation and measurements using polychromatic sources with small source-object distances

Bruno Golosio,[1,a)] Pasquale Delogu,[2] Irene Zanette,[2] Massimo Carpinelli,[1] Giovanni Luca Masala,[1] Piernicola Oliva,[1] Arnaldo Stefanini,[2] and Simone Stumbo[1]
[1]*Strutt. Dip. di Matematica e Fisica, Università di Sassari, Italy and INFN, Sez. di Cagliari, Italy*
[2]*Dipartimento di Fisica, Università di Pisa, Italy and INFN, Sez. di Pisa, Italy*

(Received 9 July 2008; accepted 10 September 2008; published online 4 November 2008)

Phase contrast imaging is a technique widely used in synchrotron facilities for nondestructive analysis. Such technique can also be implemented through microfocus x-ray tube systems. Recently, a relatively new type of compact, quasimonochromatic x-ray sources based on Compton backscattering has been proposed for phase contrast imaging applications. In order to plan a phase contrast imaging system setup, to evaluate the system performance and to choose the experimental parameters that optimize the image quality, it is important to have reliable software for phase contrast imaging simulation. Several software tools have been developed and tested against experimental measurements at synchrotron facilities devoted to phase contrast imaging. However, many approximations that are valid in such conditions (e.g., large source-object distance, small transverse size of the object, plane wave approximation, monochromatic beam, and Gaussian-shaped source focal spot) are not generally suitable for x-ray tubes and other compact systems. In this work we describe a general method for the simulation of phase contrast imaging using polychromatic sources based on a spherical wave description of the beam and on a double-Gaussian model of the source focal spot, we discuss the validity of some possible approximations, and we test the simulations against experimental measurements using a microfocus x-ray tube on three types of polymers (nylon, poly-ethylene-terephthalate, and poly-methyl-methacrylate) at varying source-object distance. It will be shown that, as long as all experimental conditions are described accurately in the simulations, the described method yields results that are in good agreement with experimental measurements. © *2008 American Institute of Physics*. [DOI: 10.1063/1.3006130]

I. INTRODUCTION

The *phase contrast imaging* technique is based on the observation of interference patterns produced when an x-ray beam partially or totally coherent crosses an object characterized by variation in the real part of the refractive index with position.[1–9] In a typical setup for this type of experiment, the radiation produced by a relatively small x-ray source acquires partial coherence during propagation in free space, crosses an object placed at relatively large distance from the source, and produces an image on an observation plane (screen). The amplitude of the interference fringes produced on the screen is particularly large around the border of structures inside the object having a refractive index different from the surrounding material. In many cases phase contrast can reveal structures that are hardly visible through absorption imaging.[4–6] The Van–Cittert–Zernike theorem[10] gives a relationship between the spatial coherence function of an electromagnetic wave and the intensity distribution of the source. In particular, the radiation produced by a quasimonochromatic and totally incoherent source becomes partially coherent at a large distance compared to the linear size of the source. In order to obtain a transverse coherence length large enough for phase contrast imaging, the distance from the source to the object should be large compared to the linear size of the source. This is the case in synchrotron facilities devoted to phase contrast imaging.[2–4,6] The possibility of phase contrast imaging using a polychromatic beam has been first demonstrated by Wilkins *et al.*,[7] who used a microfocus x-ray tube with a linear size of the source $S \simeq 20$ μm and a source-object distance $z \simeq 50$ cm. Recently, Konica Minolta Medical Imaging Inc. announced the distribution of a commercial system for phase-contrast mammography using an x-ray tube source.[11] A new generation of quasimonochromatic high-flux x-ray sources, based on the physical process of Compton backscattering, is under development.[12] These sources can be much more compact than synchrotrons and they have important potential applications in the field of phase contrast imaging. In order to optimize all the experimental parameters of phase contrast imaging systems, it is important to have reliable simulation software. For instance, in medical imaging applications the experimental parameters should be chosen so as to optimize the signal-to-noise ratio for a given value of the radiation dose delivered to the patient. However, phase contrast imaging systems based on compact sources, such as x-ray tubes or Compton backscattering sources, use source-object distances much smaller than typical distances used in synchrotron facilities. Furthermore, application of this technique to the medical field involves imaging of relatively large objects. Many approximations that are used for the simulation of phase contrast

[a)]Electronic mail: golosio@uniss.it.

 © 2008 American Institute of Physics

Downloaded 19 May 2009 to 192.167.65.36. Redistribution subject to AIP license or copyright; see http://jap.aip.org/jap/copyright.jsp

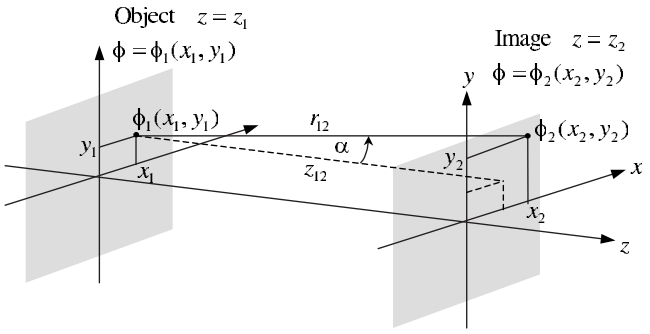

FIG. 1. Schematic diagram showing the notation used in this work. The transmitted wave function on the object plane immediately after the object is $\phi_1(\mathbf{x}_1)=\phi_0(\mathbf{x}_1)T(\mathbf{x}_1)$. The wave function on the screen $\phi_2(\mathbf{x}_2)$ can be calculated through the Fresnel–Kirchhoff equation.

imaging at synchrotron sources are not valid for this type of geometry. In the following section we describe a general method for phase contrast imaging experiment simulation based on spherical waves, which is suitable also when the approximations of large source-object distance and small transverse size of the object are not valid. In order to test the simulation method, several measurements have been done using a microfocus x-ray tube and a complementary metal-oxide semiconductor (CMOS) pixel detector in measuring the phase contrast effect on three types of plastics and varying geometrical conditions.

II. METHOD

Figure 1 shows the conventions and notation that we will use in this work:

- The coordinate origin is placed on the x-ray source.
- The object lies on an ideal plane perpendicular to the z axis and placed at distance z_1 from the source.
- The screen lies on a plane perpendicular to the z axis and placed at distance z_2 from the source and at distance $z_{12}=z_2-z_1$ from the object plane.
- A point on the object plane is represented by three coordinates in space, $\mathbf{r}_1=(x_1,y_1,z_1)$, $\mathbf{r}_1\in\mathbb{R}^3$, or by two coordinates on the plane itself $\mathbf{x}_1=(x_1,y_1)$, $\mathbf{x}_1\in\mathbb{R}^2$; the distance of this point from the source is $r_1=\|\mathbf{r}_1\|$.
- A point on the screen is represented by three coordinates in space, $\mathbf{r}_2=(x_2,y_2,z_2)$, $\mathbf{r}_2\in\mathbb{R}^3$, or by two coordinates on the screen itself $\mathbf{x}_2=(x_2,y_2)$, $\mathbf{x}_2\in\mathbb{R}^2$; the distance of this point from the source is $r_2=\|\mathbf{r}_2\|$.
- The vector joining a point on the object plane to a point on the screen is $\mathbf{r}_{12}=\mathbf{r}_2-\mathbf{r}_1$; the distance between these points is $r_{12}=\|\mathbf{r}_{12}\|$.

The simplest source that we can consider is a monochromatic dimensionless point source emitting spherical waves. The wave function of the incident radiation on the object plane is

$$\phi_0(\mathbf{x}_1)=A\frac{e^{ikr_1}}{r_1}, \tag{1}$$

where A is a constant, $k=2\pi/\lambda$ is the wave number, and λ is the wavelength of the radiation in the vacuum. A statistical source can be modeled as a superposition of independent point sources. Since there is no correlation between the waves emitted by such sources, the intensities that they produce on the screen can be calculated independently and summed up. We assume that the effect of the object on the incident wave can be completely described by its complex refractive index, which is a function of the position. This means that we consider the object homogeneous on the atomic lengthscale, thus we neglect effects due to the atomic and crystalline structures. Specifically, in case of objects made of amorphous materials, we neglect the Compton and Rayleigh scatterings. Their contribution to the intensity on the screen can be calculated independently, e.g., by Monte Carlo simulations. In case of monochromatic radiation of energy E, the complex refractive index n at the position $\mathbf{r}$ is

$$n(E,\mathbf{r})=1-\delta(E,\mathbf{r})+i\beta(E,\mathbf{r}), \tag{2}$$

where δ is the refractive index decrement and β is the absorption index, which is related to the linear absorption coefficient μ as

$$\mu(E,\mathbf{r})=2k\beta(E,\mathbf{r}). \tag{3}$$

In a compound material, δ and μ can be expressed in terms of the weight fractions w_j of the atomic elements,

$$\delta=\frac{r_e N_A\lambda^2\rho}{2\pi}\sum_j\frac{w_j(Z_j+f_j')}{A_j}, \tag{4}$$

$$\mu=N_A\rho\sum_j\frac{w_j\sigma_j}{A_j}, \tag{5}$$

where $r_e=2.82\times10^{-15}$ m is the classical electron radius, N_A is the Avogadro number, $\lambda=hc/E$ is the wavelength of the radiation in vacuum, ρ is the mass density of the material, A_j and Z_j are the atomic weight and the atomic number of the jth element, f_j' is the real part of the dispersion correction,[13] and σ_j is the total (photoelectric+Compton+Rayleigh) cross section for the interaction of a x-ray photon of energy E with the element Z_i. Values of δ and μ used in this work are obtained from the library described in Ref. 14, which is based on calculations made by Kissel *et al.*[15] and by Elam *et al.*[16] for f' and σ, respectively. If the object is thin along the radiation propagation direction, we can neglect deviation of the x-ray paths inside the object from straight lines (thin-sample approximation). Using this approximation, the effect of the object on the incident wave is entirely described by a transmission function $T(\mathbf{x}_1)$,

$$T(\mathbf{x}_1)=\int_{-\epsilon}^{+\epsilon}\exp[ikn(E,\mathbf{r}_1+\hat{\mathbf{r}}_1 s)]ds, \tag{6}$$

where the integration is made along the direction of propagation $\hat{\mathbf{r}}_1=\mathbf{r}_1/\|\mathbf{r}_1\|$ and the integration limits $\pm\epsilon$ are large enough to include the whole thickness of the object. The transmitted wave function on the object plane immediately after the object is

$$\phi_1(\mathbf{x}_1)=\phi_0(\mathbf{x}_1)T(\mathbf{x}_1). \tag{7}$$

According to the Fresnel–Kirchhoff equation, the wave amplitude on the screen (see Fig. 1) is given by

Downloaded 19 May 2009 to 192.167.65.36. Redistribution subject to AIP license or copyright; see http://jap.aip.org/jap/copyright.jsp

$$\phi_2(\mathbf{x_2}) = \int_{\mathbb{R}^2} \phi_1(\mathbf{x_1}) \frac{e^{ikr_{12}}}{i\lambda r_{12}} \cos\,\alpha d\mathbf{x_1}, \tag{8}$$

where $\phi_1(\mathbf{x}_1)$ is the wave amplitude on the object plane and α is the angle between $\mathbf{r}_{12}$ and the surface normal vector $\hat{z}$. Calculations made for experiments with synchrotron radiation often use the plane-wave approximation, i.e., ϕ_0 is assumed to be constant over the object plane. Using the plane-wave approximation and the paraxial or small-angle approximation ($\cos\,\alpha \simeq 1$), ϕ_2 can be expressed as[9]

$$\phi_2(\mathbf{x_2}) = \phi_0 T * G_{\mathrm{PW}} \tag{9}$$

where " *" denotes the convolution and G_{PW} is the propagator kernel,

$$G_{\mathrm{PW}}(\mathbf{x}) = \frac{e^{ikz_{12}}}{i\lambda z_{12}} e^{ik(\mathbf{x}^2/2z_{12})}. \tag{10}$$

The plane wave approximations is valid when the source-object distance z_1 is much greater than the object-screen distance z_{12} and than the linear size D of the object, $z_1 \gg z_{12}$ and $z_1 \gg D$. These conditions are usually fulfilled for experiments made at synchrotron facilities, however they are not valid in general for experiments made using other kind of x-ray sources, e.g., x-ray tubes. In case of a monochromatic point source emitting spherical waves [Eq. (1)], under the thin-sample approximation, the Fresnel–Kirchhoff Eq. (8) yields

$$\phi_2(\mathbf{x}_2) = A \int_{\mathbb{R}^2} T(\mathbf{x}_1) \frac{e^{ikr_1}}{r_1} \frac{e^{ikr_{12}}}{i\lambda r_{12}} \cos\,\alpha d\mathbf{x}_1. \tag{11}$$

Let $\mathbf{X}_1 = (X_1, Y_1)$ be the coordinates of the point on the object plane intersected by the straight line connecting the source to the observation point,

$$\mathbf{X}_1 = \frac{z_1}{z_2}\mathbf{x}_2, \tag{12}$$

where R_1 is the distance from the source to the intersection point, R_2 is the distance from the source to the observation point, and $R_{12} = R_2 - R_1$ is the distance from the intersection to the observation point. In a small neighborhood of the intersection point, the factor $1/r_1 r_{12}$ changes much more slowly than the phase factor and can be treated as constant and equal to $1/R_1 R_{12}$,

$$\phi_2(\mathbf{x}_2) = A \frac{\cos\,\alpha}{i\lambda R_1 R_{12}} \int_{\mathbb{R}^2} T(\mathbf{x}_1) e^{ik(r_1 + r_{12})} d\mathbf{x}_1. \tag{13}$$

A Taylor expansion of $r_1 + r_{12}$ to the second order in $\mathbf{s} = \mathbf{x}_1 - \mathbf{X}_1$ yields

$$r_1 + r_{12} = R_2 + \frac{1}{2}\left(\frac{1}{R_1} + \frac{1}{R_{12}}\right)(\mathbf{s}^2 - (\boldsymbol{\xi}\cdot\mathbf{s})^2), \tag{14}$$

where $\boldsymbol{\xi} = \mathbf{x}_2/R_2$ and it is related to the angle α as $\boldsymbol{\xi}^2 = \sin^2\,\alpha$. Substituting it in Eq. (13) yields

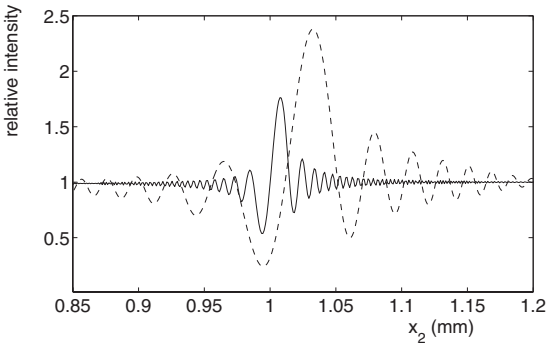

FIG. 2. Simulations made using the plane wave and the spherical wave approximations. The simulated system consists of a monochromatic point source ($E = 20$ keV), an ideal detector placed at a 50 cm distance from the source, and a 200 μm diameter nylon wire placed at a 5 cm distance from the source, with the axis perpendicular to the incident wave direction. The figure shows the interference fringes corresponding to the right border of the wire. The solid line represents the intensity obtained through the magnified plane wave approximation, while the dashed line represents the intensity obtained through the spherical approximation.

$$\phi_2(\mathbf{x}_2) = A \frac{e^{ikR_2} \cos\,\alpha}{i\lambda R_1 R_{12}} \int_{\mathbb{R}^2} T(\mathbf{x}_1) \times e^{ik/2(1/R_1 + 1/R_{12})\{(\mathbf{x}_1 - \mathbf{X}_1)^2 - [(\mathbf{x}_1 - \mathbf{X}_1)\cdot\boldsymbol{\xi}]^2\}} d\mathbf{x}_1. \tag{15}$$

Equation (15) is not a convolution of the transmission function T with a propagation kernel, essentially because $\boldsymbol{\xi}$ and α depend on the position on the screen $\mathbf{x}_2$. However, for small angles ($\alpha \ll 1$), Eq. (15) becomes

$$\phi_2(\mathbf{x}_2) = A \frac{e^{ikR_2}}{i\lambda z_1 z_{12}} \int_{\mathbb{R}^2} T(\mathbf{x}_1) e^{ik/2(1/z_1 + 1/z_{12})(\mathbf{x}_1 - \mathbf{X}_1)^2} d\mathbf{x}_1. \tag{16}$$

Besides a phase factor, Eq. (16), is the convolution of T with the propagation kernel

$$G(\mathbf{x}) = \frac{A}{i\lambda z_1 z_{12}} e^{ik/2(1/z_1 + 1/z_{12})\mathbf{x}^2} \tag{17}$$

evaluated at the point $\mathbf{X}_1 = z_1/z_2(\mathbf{x}_2)$. The factor z_1/z_2 accounts for magnification. Besides this factor, Eq. (16) differs from Eq. (9) obtained with the plane wave approximation for the factor $(1/z_1 + 1/z_{12})$ in the propagation kernel exponent, which becomes equal to $1/z_{12}$ only in the limit $z_1 \gg z_{12}$.

Figure 2 compares simulations made using the plane wave and the spherical wave approximations. The simulated system consists of a monochromatic point source ($E = 20$ keV), an ideal detector placed at a 50 cm distance from the source, and a 200 μm diameter nylon wire placed at a 5 cm distance from the source, with the axis perpendicular to the radiation direction. Even taking into account magnification, the plane-wave approximation does not yield correct results.

In the case of a polychromatic point source, the signal on the detector can be computed as

Downloaded 19 May 2009 to 192.167.65.36. Redistribution subject to AIP license or copyright; see http://jap.aip.org/jap/copyright.jsp

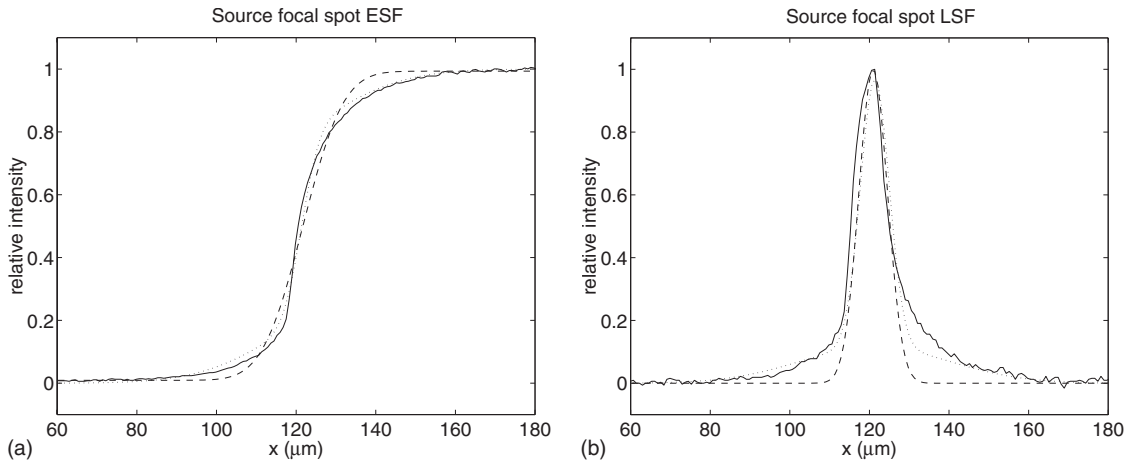

FIG. 3. Source focal spot ESF and LSF measured using the penumbra method. In (a) the solid line represents the measured profile of the ESF, the dashed line is a fit using a single erf function, the dotted line is a fit using the superposition of two erf functions. In (b) the solid line represents the LSF obtained as the derivative of the measured profile of the ESF, the dotted line is the derivative of the fit that uses two erf functions, and the dashed line is the derivative of the fit that uses a single erf function.

$$I^{\text{point}}(\mathbf{x}_2) = \int \epsilon(E)\phi_2(E,\mathbf{x}_2)\phi_2^*(E,\mathbf{x}_2)dE, \tag{18}$$

where $\epsilon(E)$ is the detector energy response. An extended incoherent source with a source distribution $I^{\text{source}}(\mathbf{x}_s)$ can be modeled as a superposition of independent point sources.[8] The intensity contribution from different points is identical except for a weighting factor $I^{\text{source}}(\mathbf{x}_s)$ and a translation given by $\mathbf{x}_s z_{12}/z_1$. The average intensity is thus equal to the convolution between the intensity of a point source and the geometrical projection of the source distribution I^{source} through the object on the detector, i.e.,

$$I(\mathbf{x}_2) = I^{\text{source}}(\mathbf{x}_2 z_1/z_{12}) * I^{\text{point}}(\mathbf{x}_2), \tag{19}$$

where the $*$ denotes the convolution.

III. RESULTS

The experimental setup for the measurements consisted of a microfocus x-ray tube and a pixel detector based on CMOS technology. The x-ray tube was a tungsten anode microfocus model 60KVMFX-SPL produced by Hamamatsu. The spectrum has been measured for different voltage (kV_p) values using the FLUXEN spectrometric system.[17] In the phase contrast imaging measurements, the voltage has been set to a fixed value of 30 kV_p. The source spot has been measured using the penumbra method.[18,19] A 40 μm thick tungsten sheet was placed between the source and the detector with the edge in the center of the field. The edge spread function (ESF), shown in Fig. 3(a), has been extracted from the image. The derivative of the ESF is the line spread function (LSF), shown in Fig. 3(b). The LSF is approximately equal to the source focal spot magnified by a factor of z_{12}/z_1. Hames *et al.*[18] and Uchida *et al.*[19] made a fit on the LSF using a Gaussian function. However, it can be observed that the LSF decreases more slowly to zero at the borders compared to a Gaussian function. A more realistic representation can be obtained by fitting the LSF using the superposition of two Gaussian functions. Since the noise in the LSF is relatively much larger than that in the ESF, due to derivative operation, the fit has been done directly on the ESF using a function of the form

$$F(x) = C_1 \operatorname{erf}\left(\frac{x-x_0}{\sqrt{2}\sigma_1}\right) + C_2 \operatorname{erf}\left(\frac{x-x_0}{\sqrt{2}\sigma_2}\right) + C_3 \tag{20}$$

where C_1, C_2, C_3, x_0, σ_1, and σ_2 are fitting parameters. Figure 3(a) compares the fit that uses a single error function (erf) to the fit that uses a superposition of two erfs. In Fig. 3(b) the derivatives of the fitting functions are compared to the LSF.

The detector was a silicon photodiode array model Rad-Eye™ 2 produced by Rad-icon Imaging Corp, containing 1024×1024 pixels at a pitch of 48 μm. The point spread function (PSF) has been measured using the edge method. The estimated value of the full width at half maximum (FWHM) was 120 ± 10 μm. In the simulations, the PSF was modeled by a Gaussian function having the same width. Phase contrast imaging measurements have been done on three types of wires: a 500 μm diameter nylon-6 wire, a 500 μm diameter poly-ethylene-terephthalate wire, and a 1 mm diameter poly-methyl-methacrylate (pmma) wire. The compositions and densities used in the simulations for those materials are the ones reported in the National Institute of Standards and Technology database.[20] The source-detector distance was fixed at 70 cm. The source-object distances were varied between 2.5 and 27.5 cm. Dark signal and flat-field images have been acquired immediately before each measurement. The raw images have been equalized by subtracting the dark signal and dividing by the flat-field signal. The scattering background contribution, due to Compton and Rayleigh scattering from the wire and the detector supports, from the wire itself and from the air, was also taken into account. It has been modeled as a uniform background superimposed on the primary signal.[21] Because of the difficulty of computing this contribution, it was evaluated from experimental measurements. The contribution of the primary radiation to the flat field signal on the detector is

Downloaded 19 May 2009 to 192.167.65.36. Redistribution subject to AIP license or copyright; see http://jap.aip.org/jap/copyright.jsp

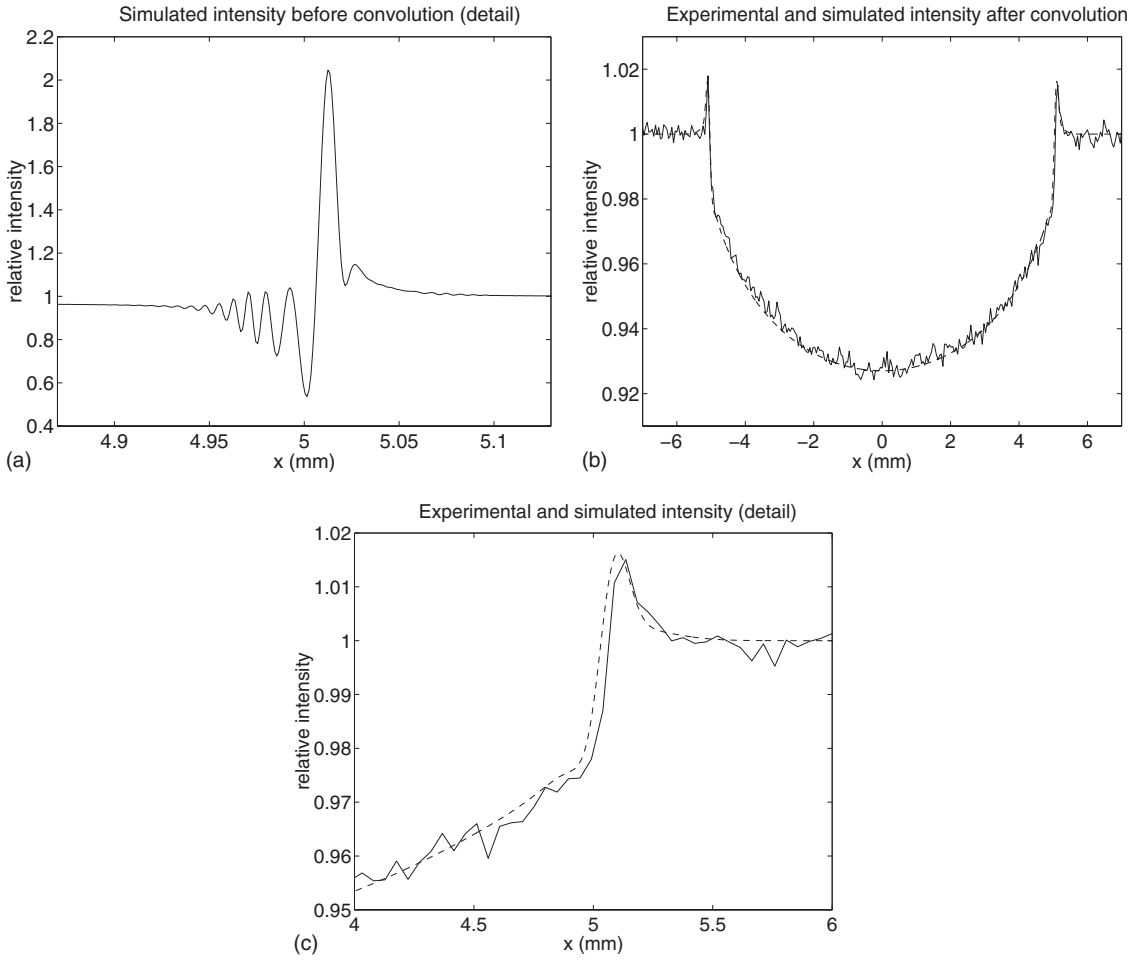

FIG. 4. Simulated and experimental signal profile of the 1 mm diameter pmma wire placed at a 5 cm distance from the source, with a source-detector distance of 50 cm. (a) Detail of the wire right border simulated signal before convolution with the PSFs due to the detector and to the source focal spot extension. (b) Comparison between the experimental signal (solid line) and the simulated signal after convolution (dashed line). The experimental signal has been corrected for the dark signal, normalized to the flat field, and averaged over 100 rows of the image acquired by the detector. (c) Detail of the wire right border experimental signal and simulated signal after convolution.

$$S_0^{\text{prim}} = F_0 \int \rho(E)\epsilon(E)dE, \tag{21}$$

where F_0 is the flat field fluence on the detector, $\rho(E)$ is the normalized spectrum, and $\epsilon(E)$ is the detector energy response. According to the Lambert–Beers law, the primary signal corresponding to the middle of the wire is

$$S^{\text{prim}} = F_0 \int \rho(E)\epsilon(E)e^{-\mu(E)d}dE = \alpha S_0^{\text{prim}}, \tag{22}$$

where $\mu(E)$ is the absorption coefficient of the wire material, d is the wire diameter, and α is the ratio between the primary signal and the primary flat-field signal. For a fixed setup and energy spectrum, the scattering background signal is proportional to the primary signal[21]

$$S^{\text{scatt}} = \beta S_0^{\text{prim}}, \tag{23}$$

where beta is the scatter-to-primary ratio. The total signal and the flat-field signal are, respectively,

$$S = S^{\text{prim}} + S^{\text{scatt}} = (\alpha + \beta)S_0^{\text{prim}}, \tag{24}$$

$$S_0 = S_0^{\text{prim}} + S^{\text{scatt}} = (1 + \beta)S_0^{\text{prim}}, \tag{25}$$

and the contrast is

$$C = \frac{S_0 - S}{S_0} = \frac{1 - \alpha}{1 + \beta}. \tag{26}$$

Solving this equation for β, we obtain

$$\beta = \frac{1 - \alpha}{C} - 1. \tag{27}$$

Using this equation, β has been evaluated for the three types of wires at a fixed source-detector distance z_2=70 cm and varying source-object distance, by computing the parameter α through Eq. (22) and evaluating the contrast C from experimental measurements. The estimated values of the scatter-to-primary ratio, β=0.18 ± 0.03, did not depend significantly on the type of wire and on the source object distance, basically because the wire itself gives a very little contribution to the total scattering background compared to the air and to other parts of the experimental system.

Figure 4 shows the experimental and the simulated signal profile of the pmma wire placed at a 5 cm distance from the source, with a source-detector distance of 50 cm. The

Downloaded 19 May 2009 to 192.167.65.36. Redistribution subject to AIP license or copyright; see http://jap.aip.org/jap/copyright.jsp

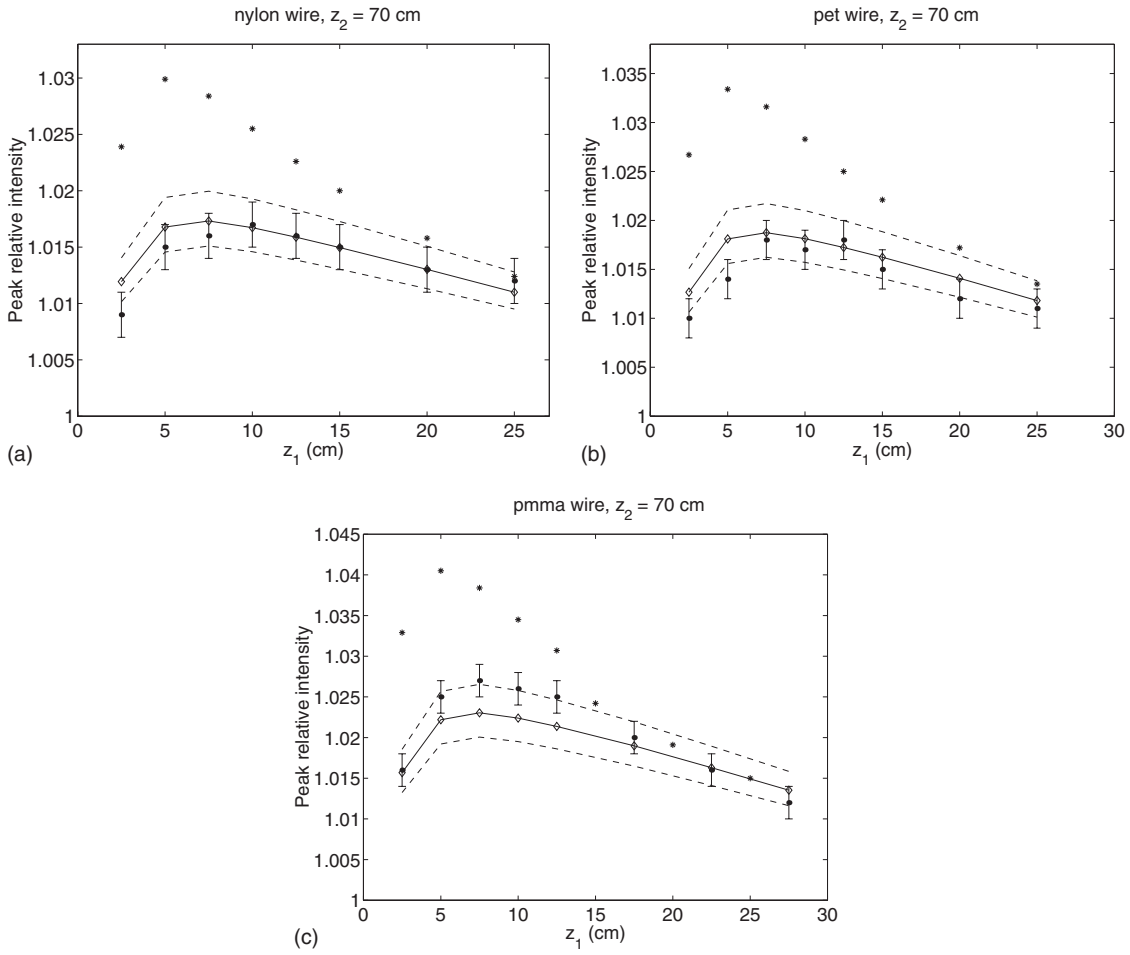

FIG. 5. Peak intensities evaluated from experimental and simulated profiles for the three types of wires at varying source-object distances. The solid lines with diamonds represent the values calculated from simulated images using a double-Gaussian model for the source focal spot. The band between the two dotted lines represents the uncertainty in those values. The stars (" ") represent the values calculated from simulated images using a single-Gaussian model for the source focal spot. The error bars represent the values determined from experimental images.

edge enhancement effect due to phase contrast is clearly visible at the borders of the wire. Figure 4(a) shows a detail of the wire right border before convolution with the PSFs due to the detector and to the source focal spot extension. In Figs. 4(b) and 4(c), the solid line represents the measured profile, corrected for the dark signal and normalized to the flat field, averaged over 100 rows of the image, while the dashed line represents the simulated profile after convolution.

For each profile we estimated the peak intensity, the peak FWHM, and the peak-to-peak distance. Figure 5 compares the peak intensities evaluated from experimental and simulated profiles for the three types of wires at varying source-object distances. The solid lines represent the values calculated from simulated images using a double-Gaussian model for the source focal spot. The band between the two dotted lines represents the uncertainty in those values. It was assumed that the main uncertainties are due to the errors in the source focal spot size and in the FWHM of the detector PSF that have been used in the simulations, while all other error sources are considered as negligible in comparison. The stars represent the values calculated from simulated images using a single Gaussian model for the source focal spot. The error bars represent the values determined from experimental images. It can be seen that within the error ranges practically all experimental values are compatible with values calculated from simulations using a double-Gaussian model, while results obtained using the single-Gaussian model are significantly different, particularly for small source-object distances. Figure 6 compares the peak FWHM evaluated from experimental and simulated profiles for the three types of wires at varying source-object distances. The measurements of the left and right side positions of the peak cannot be more precise than the detector pixel size (48 μm), therefore the error on the measured values of the FWHM (± 96 μm) is relatively large. Figure 7 shows the peak-to-peak distances evaluated from experimental and simulated profiles for the pmma wire at varying source-object distances.

IV. CONCLUSION

The simulations made using the method based on spherical waves are in good agreement with the experimental measurements made using the microfocus x-ray tube in all geometrical conditions and with all three types of samples that we used. The description of the source focal spot based on a double-Gaussian model in the simulations yields results that are compatible with experimental measurements even when the source-object distance is as small as a few centimeters,

Downloaded 19 May 2009 to 192.167.65.36. Redistribution subject to AIP license or copyright; see http://jap.aip.org/jap/copyright.jsp

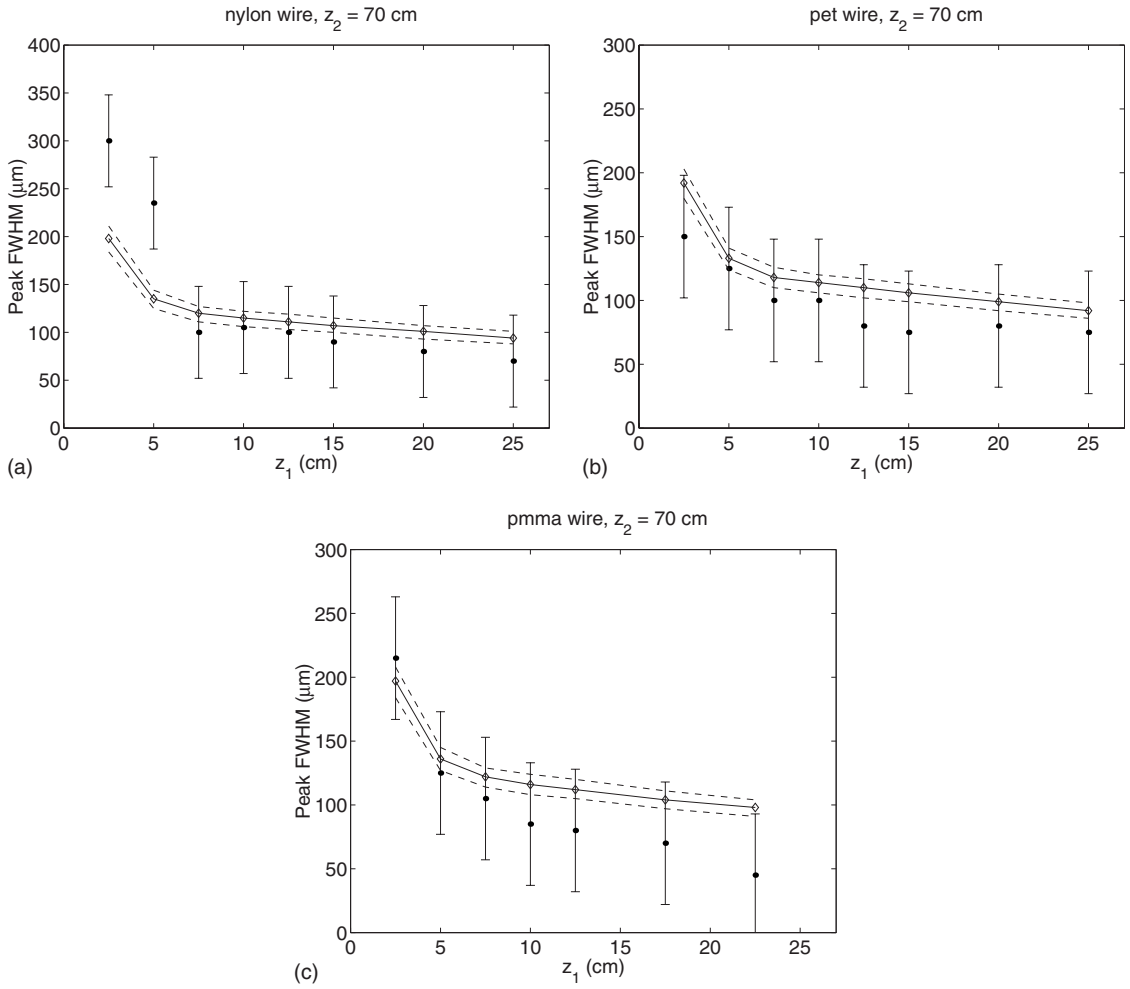

FIG. 6. Peak FWHM evaluated from experimental and simulated profiles for the three types of wires at varying source-object distances. The solid lines with diamonds represent the values calculated from simulated images. The band between the two dotted lines represents the uncertainty in those values. The error bars represent the values determined from experimental images.

while the single Gaussian model yields good results only when the source-object distance is relatively large. We can conclude that the method that we presented is suitable for the simulation of phase contrast imaging experiments in a wide range of experimental conditions, including those of compact x-ray sources.

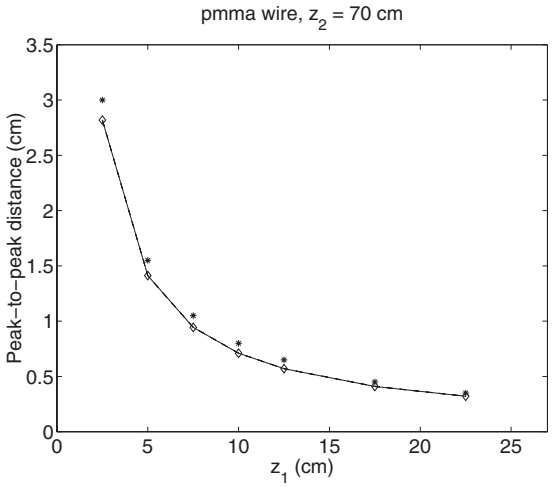

FIG. 7. Peak-to-peak distances evaluated from experimental and simulated profiles for the pmma wire at varying source-object distances. The solid line with diamonds represents the values calculated from simulated images. The stars (*) represent the values determined from experimental images.

ACKNOWLEDGMENTS

This work has been partially supported by the Italian Istituto Nazionale di Fisica Nucleare (INFN, CSN V). A part of the results reported in this paper have been produced by the Cybersar project managed from the COSMOLAB Consortium, a project partially funded from the Ministero dell'Università e della Ricerca (MIUR) by the Piano Operativo Nazionale "Ricerca Scientifica, Sviluppo Tecnologico, Alta Formazione" (PON 2000–2006).[22] We thank Dr. G. Stegel and Professor T. Steger (Struttura Dipartimentale di Matematica e Fisica, Università di Sassari, Italy), Professor U. Bottigli (Dipartimento di Fisica, Università di Siena e INFN, Sezione di Pisa, Italy), Dr. I. Bukreeva, Dr. A. Cedola, and Dr. S. Lagomarsino [Istituto di Fotonica e Nanotecnologie (IFN)-CNR-Roma, Italy] for their support and useful discussion, and Gavino Cherchi for his support for the installation and configuration of the computer cluster.

Downloaded 19 May 2009 to 192.167.65.36. Redistribution subject to AIP license or copyright; see http://jap.aip.org/jap/copyright.jsp

[1]T. J. Davis, D. Gao, T. E. Gureyev, A. W. Stevenson, and S. W. Wilkins, Nature (London) **373**, 595 (1995).
[2]A. Snigirev, I. Snigireva, V. Kohn, S. Kuznetsov, and I. Scelokov, Rev. Sci. Instrum. **66**, 5486 (1995).
[3]P. Cloetens, R. Barret, J. Baruchel, J. P. Guigay, and M. Sclenker, J. Phys. D **29**, 133 (1996).
[4]F. Arfelli, M. Assante, V. Bonvicini, A. Bravin, G. Cantatore, E. Castelli, L. D. Palma, M. D. Michiel, R. Longo, A. Olivo, S. Pani, D. Pontoni, P. Poropat, M. Prest, A. Rashevsky, G. Tromba, A. Vacchi, E. Vallazza, and F. Zanconati, Phys. Med. Biol. **43**, 2845 (1998).
[5]V. N. Ingal, E. A. Beliaevskaya, A. P. Brianskaya, and R. D. Merkurieva, Phys. Med. Biol. **43**, 2555 (1998).
[6]P. Cloetens, M. Pateyron-Salomé, J. Y. Buffière, G. Peix, J. Baruchel, F. Peyrin, and M. Sclenker, J. Appl. Phys. **81**, 5878 (1997).
[7]S. W. Wilkins, T. E. Gureyev, D. Gao, A. Pogany, and A. W. Stevenson, Nature (London) **384**, 335 (1996).
[8]P. Cloetens, Ph.D. thesis, Vrije Universiteit Brussel, 1999.
[9]T. Weitkamp, *Imaging and Tomography with High Resolution Using Coherent Hard Synchrotron Radiation* (Cuvillier, Göttingen, 2002).
[10]M. Born and E. Wolf, *Principles of Optics* (Pergamon, Oxford, 1975).
[11]Konica Minolta Medical and Graphic, Inc., Phase contrast technology, http://www.konicaminolta.com/healthcare/technology/phasecontrast
[12]K. Dobashi, M. Uesaka, A. Fukasawa, H. Iijima, J. Urakawa, T. Higo, M. Akemoto, and H. Hayano, Proceedings of the EPAC 2002, Paris, France, 2002 (unpublished), pp. 677–679.
[13]L. G. Parratt, Phys. Rev. **95**, 359 (1954).
[14]A. Brunetti, M. S. del Rio, B. Golosio, A. Simionovici, and A. Somogyi, Spectrochim. Acta, Part A **59**, 1725 (2004).
[15]L. Kissel, B. Zhou, S. C. Roy, S. K. S. Gupta, and R. H. Pratt, Acta Crystallogr., Sect. A: Found. Crystallogr. **51**, 271 (1995).
[16]W. T. Elam, B. D. Ravel, and J. R. Sieber, Radiat. Phys. Chem. **63**, 121 (2002).
[17]S. Stumbo, U. Bottigli, B. Golosio, P. Oliva, and S. Tangaro, Med. Phys. **31**, 2763 (2004).
[18]S. M. Hames, M. J. Flynn, and D. A. Reimann, Nuclear Science Symposium and Medical Imaging Conference, 1992 (unpublished), Vol. 25, p. 1331.
[19]H. Uchida, K. Hasuike, K. Torii, and H. Tsunemi, Jpn. J. Appl. Phys., Part 1 **45**, 5277 (2006).
[20]National Institute of Standards and Technology, x-ray mass attenuation coefficients, http://physics.nist.gov/PhysRefData/XrayMassCoef/tab2.html
[21]S. Webb, *The Physics of Medical Imaging* (Institute of Physics, Bristol, 1993).
[22]More information is available on web page http://www.cybersar.com

Downloaded 19 May 2009 to 192.167.65.36. Redistribution subject to AIP license or copyright; see http://jap.aip.org/jap/copyright.jsp